JMEPEG (2007) 16:404–417
DOI: 10.1007/s11665-007-9060-0

1059-9495/$19.00

Friction Stir Processed AA5182-O and AA6111-T4 Aluminum Alloys. Part 2: Tensile Properties and Strain Field Evolution

Louis G. Hector Jr., Yen-Lung Chen, Sumit Agarwal, and Clyde L. Briant

(Submitted January 10, 2007; in revised form February 11, 2007)

In this second part, a state-of-the-art digital image correlation (DIC) technique was used to compute true stress-true strain curves beyond diffuse necking for friction stir processed AA5182-O and AA6111-T4 aluminum alloys. Of particular interest were differences in key tensile properties, such as initial yield point, and ultimate tensile strength, between the base and friction stir processed materials. Tensile coupons cut from the same material used to investigate crystallographic texture via the electron backscatter diffraction technique in Part 1, were strained to failure in a miniature tensile stage. The evolution of two-dimensional strain fields in both the base and friction stir processed materials was explored with incremental and cumulative strain maps computed from digital grids superimposed on each image after testing was completed. The impact of friction stir processing on strain localization just prior to fracture was revealed through changes in incremental strain map contour profiles. It is suggested that grain size refinement due to friction stir processing has a prominent effect on strength, while texture plays a secondary role.

Keywords AA5182-O, AA6111-T4, digital image correlation, friction stir, strain tensile testing, ultimate tensile strength, yield strength

1. Introduction

In Part 1 (Ref 1), crystallographic texture in friction stir processed AA5182-O and AA6111-T4, two important aluminum automotive alloys, was examined with electron backscattered diffraction (EBSD) (Ref 2). Using electrical discharge machining, coupons were cut from the friction stir processed zones along directions parallel and perpendicular to the direction of tool translation. Thin slices were also cut through the friction stir processed zones (i.e., perpendicular to the top surface or surface that was in contact with the tool) to explore through-thickness texture variations. Texture measurements were made at key positions along the surfaces of each coupon and differences between the two Al alloys discussed in detail. It was determined that texture was primarily localized on the top surface of the coupons examined and the texture became weaker with increasing depth. Both materials showed significant differences in grain size and texture between the advancing and retreating sides of the friction stir processed zone. The advancing side had a smaller grain size than the retreating side. In general, the texture was stronger on the advancing side than on the retreating side and poles were rotated in the direction of tool rotation when going from one side to the other. The overall texture is stronger in the AA6111-T4 material than in the AA5182-O material. This appears to be a material effect because similar observations were made when comparing laser welds in these materials (Ref 3).

A direct linkage between mechanical properties and texture of friction stir processed AA5182-O and AA6111-T4 alloys will ultimately be required for better process and material understanding. However, the subtle variations in texture across the friction stir processed zones (as noted in Part 1) and their impact on local mechanical properties would in fact require a comprehensive investigation involving very small tensile coupons (for example) cut from specific texture regions. While this is in principle possible, we chose to investigate tensile properties of coupons consisting almost entirely of friction stir processed material of both alloys. We believe that this is the necessary first step toward establishing a quantitative linkage between texture and mechanical properties of friction stir processed aluminum alloys.

A series of quasi-static tensile tests was therefore conducted with both friction stir processed and base AA5182-O and AA6111-T4 alloys. We used the same materials and coupon geometries as those used in the EBSD analysis of Part 1 (Ref 1). Key tensile properties of friction stir processed AA5182-O and AA6111-T4 materials were measured and compared with the corresponding base materials. Of particular interest was the extent to which friction stir processing alters tensile properties (e.g., yield stress and ultimate tensile strength) and true stress-true strain in tension beyond diffuse necking. A state-of-the-art digital image correlation (DIC) technique, wherein strain fields from images recorded during a tensile test are computed with a

This article was presented at Materials Science & Technology 2006, Innovations in Metal Forming symposium held in Cincinnati, OH, October 15-19, 2006.

Louis G. Hector Jr., and **Yen-Lung Chen,** General Motors Research and Development Center, 30500 Mound Road, Warren, MI 48090; **Sumit Agarwal,** Applied Materials, Inc., 21515 N.W. Evergreen Parkway, Hillsboro, OR 97124; **Clyde L. Briant,** Brown University, Providence, RI 02912. Contact e-mail: louis.hector@gm.com.

digital strain gage, provided a series of color contours or strain maps from which were extracted the true stress-true strain behavior. The evolution of axial (i.e., parallel to the tensile axis) and transverse (i.e., perpendicular to the tensile axis) strain fields in each material was examined with both cumulative strain contour maps (which compare temporally distant images) and incremental strain contour maps (which compare images recorded in temporal succession). Differences in dynamic strain aging in the AA5182-O base and friction stir processed materials as manifested, for example, by propagating bands of plastic deformation (often referred to as the Portevin-LeChâtelier effect), were explored. We note that DIC has previously been applied to investigate mechanical properties of aluminum alloys AA2024 (Ref 4) and AA2524 (Ref 5).

The remainder of this article is organized as follows. In Section 2, we summarize experimental details associated with the tensile tests and digital image correlation technique. In Section 3, the measured tensile properties are reported and a detailed investigation of strain field evolution in the base and friction stir processed materials is presented through selected incremental and cumulative strain maps. The major results of this investigation are summarized in Section 4.

2. Experimental

2.1 Tensile Coupon Geometry/Preparation

The tensile coupon geometry selected for this investigation consisted of a gage section that follows a continuous radius with an approximate 9° taper. This is shown in Fig. 3(a) of Part 1 (Ref 1). Although this geometry guarantees strain localization and fracture at the center of the gage section, it also induces a slight biaxial stress state in contrast to a straight gage section. This results in a small overestimate of the tensile properties such as the yield and ultimate tensile strengths when using rectangular digital grids. However, proper placement of the digital grid on the necking region during image correlation greatly reduces this error. In addition, investigation of strain evolution at the highest possible spatial resolution with digital image correlation is feasible since grid placement is known a priori (i.e., only the necking region needs to be imaged with the camera) leading to maximum pixel densities. Similar tests with straight gage section coupons (i.e., coupons with no intentional taper, not discussed in the present article) suggest that the tapered geometry leads to tensile strengths that are 1-5% in excess of those from the straight gage section.

Prior to tensile testing, one surface of each tensile coupon was decorated with a high density of unique contrast features. Although different application techniques are possible, what was found to work best for the DIC analysis of the Al tensile coupons was the application of a dense coating of white spray paint droplets, followed by a less dense coating of black spray paint droplets.

2.2 Tensile Stage and Image Acquisition System

All coupons were strained to fracture in a miniature tensile testing stage, with associated load and displacement controller, shown in Fig. 1. The tensile stage was manufactured by Kammrath-Weiss in Dortmund, Germany (Ref 6). One revolution of the screws produces 2 mm of cross-head displacement. The tensile coupons were positioned in the grips of the testing stage (as shown in Fig. 1b), clamped with hardened steel "bite plates" and pulled at one end until fracture. A fiber optic light source was positioned to provide a low level of illumination. The tests were conducted at a cross-head speed of 0.020 mm/s corresponding to a nominal strain rate of 10^{-3}/s. During each test, the axial load, measured with a 5 kN load cell, and displacement, measured with the displacement transducer shown in Fig. 1(b), were recorded using a data acquisition system at a sampling rate of 3 Hz. Digital images of the gage section were captured every 2 s by a SONY CCD camera mounted approximately 22 cm above the testing stage and aligned with the coupon gage section. The camera had a framing rate of 7 frame/s and a pixel density of 1280×960. A telecentric lens affixed to the camera (shown in Fig. 1a), allowed image capture of the entire gage section or a portion of the gage section near its center (for example), where localization and fracture were anticipated. The lens also eliminated magnification-induced distortions across the field of view of the camera. Image intensity and depth of field were controlled with the lens f-stop, adjusted to 4, which allowed the desired amount of light into the camera. The image exposure time (typically 1/32 s) was adjusted through the image acquisition software. The pixel resolution in each recorded digital image was 0.011 mm/pixel.

The DASYLab software package (Ref 7) was used to drive the camera and to record the axial load and displacement data corresponding to each digital image captured. The software triggered the digital camera at 10 s intervals or if the force fluctuations exceeded +10% or −2% during load sampling. This technique has proven useful for the capture of serrated flow during tensile testing of certain alloys (e.g., Al-Mg alloys).

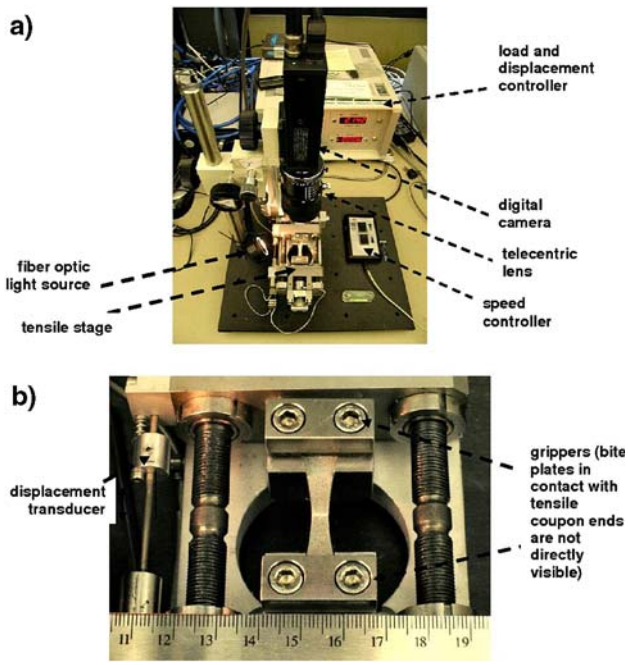

Fig. 1 Miniature tensile testing apparatus and digital camera (a) Monochrome digital camera with telecentric lens focused on a tensile coupon. Tensile stage with load cell (front), controller (white box with digital display in background), and speed controller (mouse with two buttons to the right of the tensile stage) are also shown. (b) Tensile stage with a tensile coupon moments after fracture. Note the displacement transducer on the left side of the stage

Once an image was captured by the camera, it was saved with a C++ program which assigned a sequential file name to the image and then saved it in bitmap format. When all of the images for a given test were acquired, the DASYLAb program commanded an Excel-Visual Basic program to create a folder on the DASYLab PC (the image acquisition and storage process involved 2 PCs) with the name of the test and a time stamp, and then moved the image files from the image capture PC to the newly created folder on the DASYLab PC.

2.3 Digital Image Correlation

Two-dimensional digital image correlation (DIC) is a fast and precise method for measuring in-plane deformation and displacement fields of plastically deforming sheet metals. The input to the correlation algorithm requires a set of digital images that store the deformation history recorded from one surface of the tensile coupon up to fracture. Once a test is completed, the images can then be compared in a cumulative fashion, in which an earlier image is compared with a later image, or in an incremental fashion, in which temporally successive image pairs are compared to produce deformation and displacement history. Prior applications of the DIC technique of relevance to the present study involved stress-strain characterization (up to fracture) of miniature dual-phase steel spot welds (Ref 8), and measurement of Portevin-LeChâtelier band propagation during tensile deformation of an Al-Mg alloy with a high-speed digital camera (Ref 9). The digital correlation analyses of all test results were conducted with the SDMAP3D program detailed in Ref (10, 11).

Displacement fields were computed from comparisons between contrast features in pairs of digital images before and after the application of a strain increment. More specifically, the physical problem of measuring in-plane displacements at a point in a digitally superimposed grid on a macroscopically flat surface is formulated in terms of minimization of a correlation function over a subset image region containing the grid point with respect to six deformation mapping parameters. These parameters, which are constant for each subset region, are two in-plane displacement parameters, $u(x,y)$, $v(x,y)$, which represent axial and transverse displacement fields, respectively, and four spatial derivatives, viz., $u_x(x,y)$, $u_y(x,y)$, $v_x(x,y)$, and $v_y(x,y)$, where the subscripts denote differentiation with respect to the corresponding spatial coordinate. They vary spatially from grid point to grid point, and hence form the two-dimensional whole field displacement and strain maps.

The process of computing the whole field displacement and strain maps involves two steps. In the first step, the images are recorded at prescribed intervals during the deformation process, reduced to grayscale, and then saved as raw data files of brightness values. In the second step, the region of interest in the digital images is then defined with a set of grid points (similar to nodes in a finite element mesh) that lie at the center of user-specified subset arrays (or small area elements) within each image. The six mapping parameters are then computed at each grid point. Additional post-processing filtering and smoothing is then used to compute the translation, rotation, extension, and shear of each subset. The in-plane true strain components, ϵ_1, ϵ_2, and ϵ_{12} at each load step are then computed incrementally from a consecutive set of digital images.

Four strain measures, detailed in the Appendix, were used to convert the two-dimensional strain data measured with DIC into uniaxial strain. Each strain measure was computed from a different region of the coupon gage section.

3. Tensile Properties and Strain Field Evolution

Four sets of tensile coupons (with five in each set) were strained to failure in the miniature tensile tester. These included base and friction stir processed AA5182-O and AA6111-T4 materials. Digital grids with an 89×48 density or 4272 grid points were used to compute both incremental and cumulative strain maps along with true stress-true strain data in each case. This grid density provided an adequate balance between spatial resolution and the computed strain accuracy. The strain maps are color contours of axial strain (i.e., along the tensile axis) and transverse strain (i.e., perpendicular to the tensile axis). We noted that successive tests on each coupon type yielded incremental and cumulative strain maps that were very similar, and hence we focused on results from selected coupons to illustrate salient features of each material as well as to highlight differences between the materials. Image totals per test ranged from 85 to 100 depending upon the point of fracture.

3.1 Tensile Properties of Base and Friction Stir Processed Materials

Nominal peak tensile load values recorded during tensile testing are listed in Table 1. Relative to the base materials, peak loads increased by 10% and 20% in the friction stir processed AA5182-O and AA6111-T4 materials, respectively. Nominal values of the 0.2% yield strength and ultimate tensile strength for the base and friction stir processed materials measured in the present work are listed in Table 2 and 3. Table 2 shows that there is a greater difference between the yield strengths for the AA6111-T4 materials (i.e., base and friction stir processed) than the AA5182-O materials. The 0.2% yield and ultimate strength values for AA5182-O (AA6111-T4) friction stir processed material exceed the corresponding base material values by no more than 5(14) MPa and 39(89) MPa, respectively. Measured peak strain values for base (friction stir processed) AA5182-O and AA6111-T4 were 45% (42%) and 40% (52%), respectively, as computed from $\bar{\varepsilon}_1^{(3)}$ (Eq A3). For both alloys, the yield strength is largest in the friction stir processed material. A similar observation applies for the ultimate tensile strength values listed in Table 3, although the relative differences are larger than those observed for the yield strength. We note that other tensile values have been reported in the literature. For example, Miles et al. (Ref 12) reported 0.2% yield stress and ultimate tensile strength values for base (friction stir processed) AA5182-O of 131(285.4) MPa and 138.2(285.7) MPa, respectively. An ultimate tensile strength of 178.1 MPa at 20 °C was reported in Ref (13) for base AA6111-T4. No tensile properties for friction stir processed AA6111-T4 could be located in the literature.

Figures 2 and 3 show the computed true stress-true strain curves from the four strain measures described in the Appendix. In Fig. 2, the curves for the AA5182-O base material fall below those of the AA6111-T4 material with the peak tensile strains due to $\bar{\varepsilon}_1^{(3)}$ and $\bar{\varepsilon}_1^{(5)}$ exceeding 40% for both materials. The same trend holds for the curves associated with the friction stir processed materials in Fig. 3. However, the peak stress and strain values increased by nearly 100 MPa (flow stress) and

Table 1 Peak tensile loads

Material	Peak load, N
5182-O Base	2777
5182-O FSW	3058
6111-T4 Base	3164
6111-T4 FSW	3800

Table 2 Nominal 0.2% yield strength (MPa) values from digital image correlation analysis

Material	$\bar{\varepsilon}_1^{(1)}$	$\bar{\varepsilon}_1^{(2)}$	$\bar{\varepsilon}_1^{(3)}$	$\bar{\varepsilon}_1^{(5)}$
5182-O Base	133.4	136.2	138.9	139.0
5182-O FSP	138.3	138.4	139.2	139.3
6111-T4 Base	179.1	180.0	181.2	182.3
6111-T4 FSP	192.7	193.8	194.0	194.3

FSP = friction stir processed

Table 3 Nominal ultimate tensile strength (MPa) values from digital image correlation analysis

Material	$\bar{\varepsilon}_1^{(1)}$	$\bar{\varepsilon}_1^{(2)}$	$\bar{\varepsilon}_1^{(3)}$	$\bar{\varepsilon}_1^{(5)}$
5182-O Base	282.0	291.1	292.4	293.8
5182-O FSW	320.5	318.2	325.3	330.9
6111-T4 Base	371.0	372.5	382.6	385.7
6111-T4 FSW	442.0	437.5	470.2	474.5

FSP = friction stir processed

10%, respectively, for the AA6111-T4 material. On the other hand, there is less difference between the stress-strain curves for the AA5182-O materials when comparing Fig. 2 and 3.

The most conservative measure of true stress is computed from $\bar{\varepsilon}_1^{(1)}$. This is conservative from the standpoint that the cross-sectional area is averaged over the necking region and surrounding regions that are elastically loaded. Hence, the true stresses corresponding to the green curves in both Fig. 2 and 3 decrease at smaller true strains values since the rate of decrease of the cross-sectional area of the coupon is slower than the rate of decrease in the load (which becomes localized in the necking region beyond diffuse necking). Such is not the case, however, for the other curves wherein strain measurement is more localized. For example, $\bar{\varepsilon}_1^{(3)}$, is computed along a line through the thinnest section of the necking region. The curves in Fig. 2 and 3 effectively bound reality from the standpoint that the true stress-true strain variation $\bar{\varepsilon}_1^{(1)}$ lies between the curves corresponding to $\bar{\varepsilon}_1^{(1)}$ and $\bar{\varepsilon}_1^{(5)}$, with $\bar{\varepsilon}_1^{(3)}$ thought to be the most accurate.

3.2 Strain Maps

To investigate possible differences in the strain evolution during tensile deformation between the different materials, we computed a series of strain maps which are contours of constant strain derived from surface displacement measurements from DIC. Although shear strain contours are available, we limited our investigation to axial and transverse strain maps. Strain evolution is investigated over very short time intervals with incremental strain maps and over longer periods with cumulative strain maps. Every attempt was made to correlate strains over a 4 mm × 8 mm (i.e., transverse vs. axial) region of the coupon surface with the center of the resulting strains maps coincident with the coupon center. Some variation in the size of the contour plots in the ensuing discussion resulted from scaling associated with the corresponding color keys that list numerical values of the contours (labeled Er1 or Er2, which designate computed axial and transverse strain contour values, respectively).

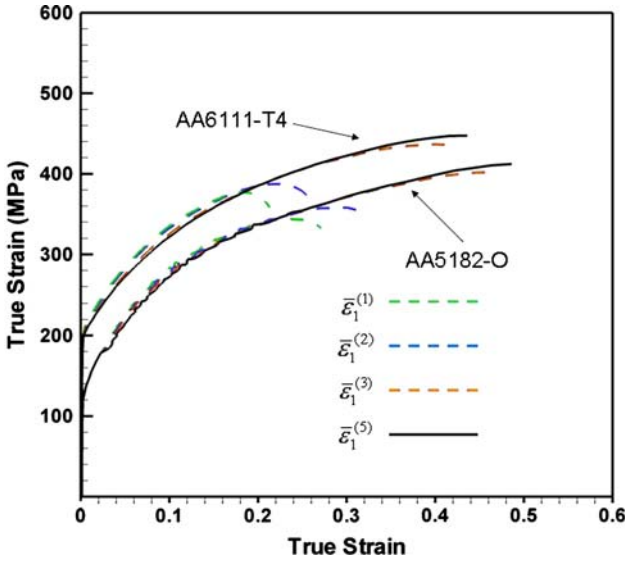

Fig. 2 True stress-true strain curves for base AA5128-O and AA6111-T4 derived from the four uniaxal strain measures listed in the Appendix

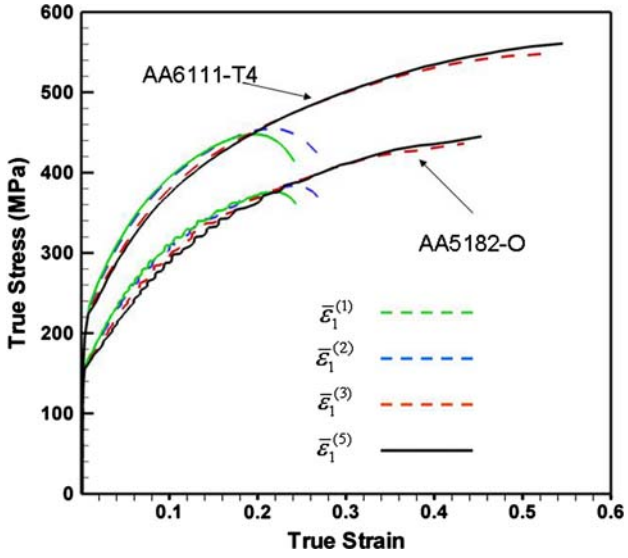

Fig. 3 True stress-true strain curves for friction stir processed AA5128-O and AA6111-T4 derived from the four uniaxial strain measures listed in the Appendix

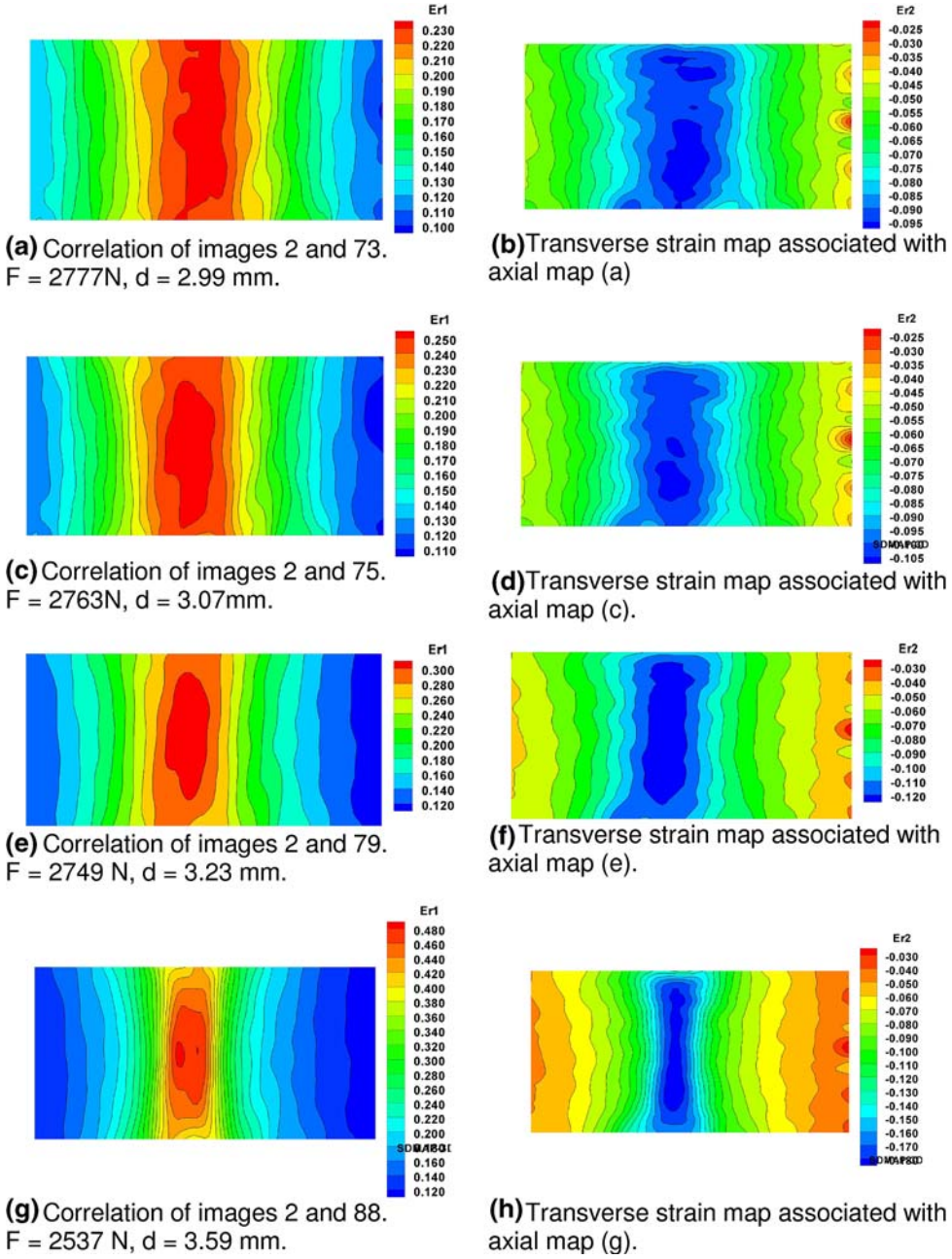

Fig. 4 Selected cumulative strain maps from DIC analysis of AA5182-O base material (prior to fracture). Tensile axis is along the horizontal. Corresponding load and cross-head displacement are denoted by F and d, respectively. (a) Correlation of images 2 and 73. F = 2777 N, d = 2.99 mm; (b) Transverse strain map associated with axial map (a); (c) Correlation of images 2 and 75. F = 2763 N, d = 3.07 mm; (d) Transverse strain map associated with axial map (c); (e) Correlation of images 2 and 79. F = 2749 N, d = 3.23 mm; (f) Transverse strain map associated with axial map (e); (g) Correlation of images 2 and 88. F = 2537 N, d = 3.59 mm; and (h) Transverse strain map associated with axial map (g)

3.2.1 AA5182-O Base. Figure 4 shows a set of cumulative strain maps taken from an AA5182-O base material coupon starting at the point of peak cross-head load (2777 N) recorded during the test. The reference image for the correlation process was image 2, as indicated in the figure captions. Figure 4(a) and (b) shows axial and transverse strain maps at the peak load. We note from the color key in Fig. 4(a) that the red contours correspond to a peak true strain of 23%, while compressive strains up to −9.5% accumulated in the same necking region as indicated in Fig. 4(b). The total cross-head displacement is 2.99 mm. Peak axial strains continued to increase in the diffuse neck region, as suggested by the 25% and 30% values listed in the keys of Fig. 4(c) and (e), as the cross-head load started to decrease. A similar observation applies for the transverse strain contours in Fig. 4(d) and (f) with compressive strains reaching −10.5% and −12%, respectively. The necking region also started to thin down as shown in Fig. 4(e) and (f). Just prior to fracture, the neck region further thinned as indicated in Fig. 4(g) wherein a 48% peak axial strain level was recorded at a total cross-head displacement of 3.59 mm. Peak compressive strains

in Fig. 4(h) were computed at −18%. A review of Fig. 4(a), (c), (e), and (g) reveals that the peak strain levels remained concentrated in a diffuse neck close to the center of the coupon for the duration of the test.

Selected incremental strain maps for the same AA5182-O base material coupon are shown in Fig. 5. It is important to emphasize that the incremental contour maps are essentially snap shots of strain increments between images recorded in temporal succession. The resolution of what are continuously changing strain fields is very much dependent upon the camera framing rate and the image acquisition rate. Faster capture rates will provide more detail between the strain increments (see Ref. 9, for example). Eight contour maps are shown for both the axial and transverse strain fields resulting from comparison of images recorded before and after the peak cross-head load was achieved (at image 73). More incremental strain maps are presented to illustrate the apparent movement of the plastic strain localization region in response to successive load increments. In the figure captions for each axial map, the measured cross-head load and displacement increments are listed as ΔF and Δd, respectively. Note that Er1 = ΔEr1 and Er2 = ΔEr2 for all incremental maps. Duplicate values in the incremental strain map keys imply strain increments of 0.0005. Figure 5(a) and (b) show a diffuse neck near the center of the coupon with peak axial and transverse strain increments of 1.4% and −0.7%, respectively. The computed $\bar{\varepsilon}_1^{(3)}$ value of 18.3% is included in the Fig. 5(a) caption for reference. However, the 20 N load increment between images 66 and 67 caused strains to localize in a band that appears on the right side of the contour plots in Fig. 5(c) and (d). Peak strain increments (listed in the keys to the right of each map) differed little from those in Fig. 5(a) and (b). A subsequent 21 N load increment returned the localization region closer to the coupon center as suggested by the incremental contour plots in Fig. 5(e) and (f). However, the shape of the strain localization region changed from the oval shape in Fig. 5(a) to a band that extended across the gage section width. Peak strain increments differed little from those in the preceding incremental maps. The axial and transverse incremental maps in Fig. 5(g) and (h), due to a 13 N load increment, suggest the development of two crossing strain bands (similar to those shown in Fig. 5a, b) with a central peak strain region denoted by the red contours in Fig. 5(g). This is perhaps best seen in Fig. 5(h) which shows what appears to be part of a band crossing as denoted by the green contours of transverse strain increment (all compressive). The maps in Fig. 5(i) and (f) are a first look at the incremental axial and transverse strain fields beyond the peak cross-head load. Interestingly, plastic strain increments are localized into a single band, with peak axial and transverse strain increments at 1.1% and −0.5%, respectively. Any hint of band crossing (suggested in Fig. 5h, for example) has vanished. A load decrement of 7 N between images 78 and 79 leads to a change in the orientation of the plastic strain band relative to the tensile axis as shown in Fig. 5(k) and (l). This resulted from peak axial and transverse strain increments of 1.5% and −0.6%, respectively. By image 80, the cross-head load dropped to 2738 N, and an 11 N load decrement associated with image 81 led to the centrally located necking region shown in Fig. 5(m) and (n). The computed $\bar{\varepsilon}_1^{(3)}$ value of 43% is included in the Fig. 5(m) caption. Just prior to fracture, a −37 N load decrement between images 86 and 87 (90 bitmap images were captured during this test), resulted in what appears to be a bi-modal strain field in the necking region positioned near the center of the coupon, as shown in Fig. 5(o). The peak axial strain decrement in this case was −3.0% and that recorded in the transverse strain map was −0.7%. We surmise that the apparent movement of contours associated with peak strain increments in the material is related to propagating bands of localized plastic strains that are indicative of dynamic strain aging (DSA) in the material. For additional details on DSA, the reader is referred to Ref. (14-16).

3.2.2 AA5182-O: Friction Stir Processed. Figure 6 shows selected cumulative strain maps from a tensile coupon consisting of AA5182-O friction stir processed material. The reference image in all cases was image 1. The peak cross-head load was 3058 N at image 86 (100 bitmap images were recorded during this test). Peak axial strain contours localized in a small region near one of the gage section edges (indicated by the orange-red contours in Fig. 6a) at a cross-head load and displacement of 3037 N and 3.24 mm, respectively. The development of a neck region is evident by the concentrated yellow contours in the axial map with corresponding cumulative strains of 21-22%. Cumulative transverse strains reached −10% in the same region. Figure 8(c) and (d) shows that the necking region continued to accumulate plastic strains in the same region as that denoted in Fig. 6(a) and (b). Peak axial strains reached 27% and 31% in Fig. 6(c) and (d), respectively, which correspond to cross-head loads of 3052 N and 3038 N, respectively. Peak transverse strains reached 11.5% and −14% in Fig. 6(d) and (f), respectively. Correlation of images 1 and 96, which represents the strain accumulation at a cross-head load of 2831 N, shows the development of a bi-model necking region with lobes of peak plastic strains at 44% and 42%, respectively. These are separated by a contour patch at 40% true strain. A similar contour profile is not noted in the transverse strain map shown in Fig. 6(h) wherein contours of peak transverse strain occurred in a vertically oriented blue contour patch at −18% strain.

Selected incremental strain maps for the same AA5182-O friction stir processed material coupon are shown in Fig. 7. As was the case for the AA5182-O base material, we present eight axial and eight transverse incremental maps generated from data collected at various points in the test. Qualitative comparison of the strain maps in Fig. 7 with those in Fig. 5 for the base material shows that the friction stir processed material never developed the oval-shaped strain localization region. Rather, strains localized in a band that traverses the width of the correlation region. For example, a developing band of plastic strain due to a 21 N load increment between images 69 and 70 is shown in the axial contour plot of Fig. 7(a). The peak axial strain increment, which corresponds to the red contour patch, is 0.9%, while the peak transverse strain increment shown in Fig. 7(b) is −0.4%. The computed $\bar{\varepsilon}_1^{(3)}$ value of 18.6% is included in the Fig. 7(a) caption. The 8 N load decrement between images 73 and 74 (some load oscillation was noted prior to the peak load point) resulted in the obvious change in band orientation relative to the tensile axis, as indicated in Fig. 7(c) and (d). It is interesting to note that there is a small orange contour near the top of the band in Fig. 7(c) that is separated from the main contour patch with a 1.0% strain increment (yellow contours). A load increment of 5 N between images 77 and 78 resulted in a change in the location of the peak axial strain increment in the direction of the small orange contour patch denoted in Fig. 7(c), with a change in the gross shape of the band in Fig. 7(e) and (f). Peak transverse strain increments computed for this load increment were in upwards of 0.7% as shown in Fig. 7(f). Although the

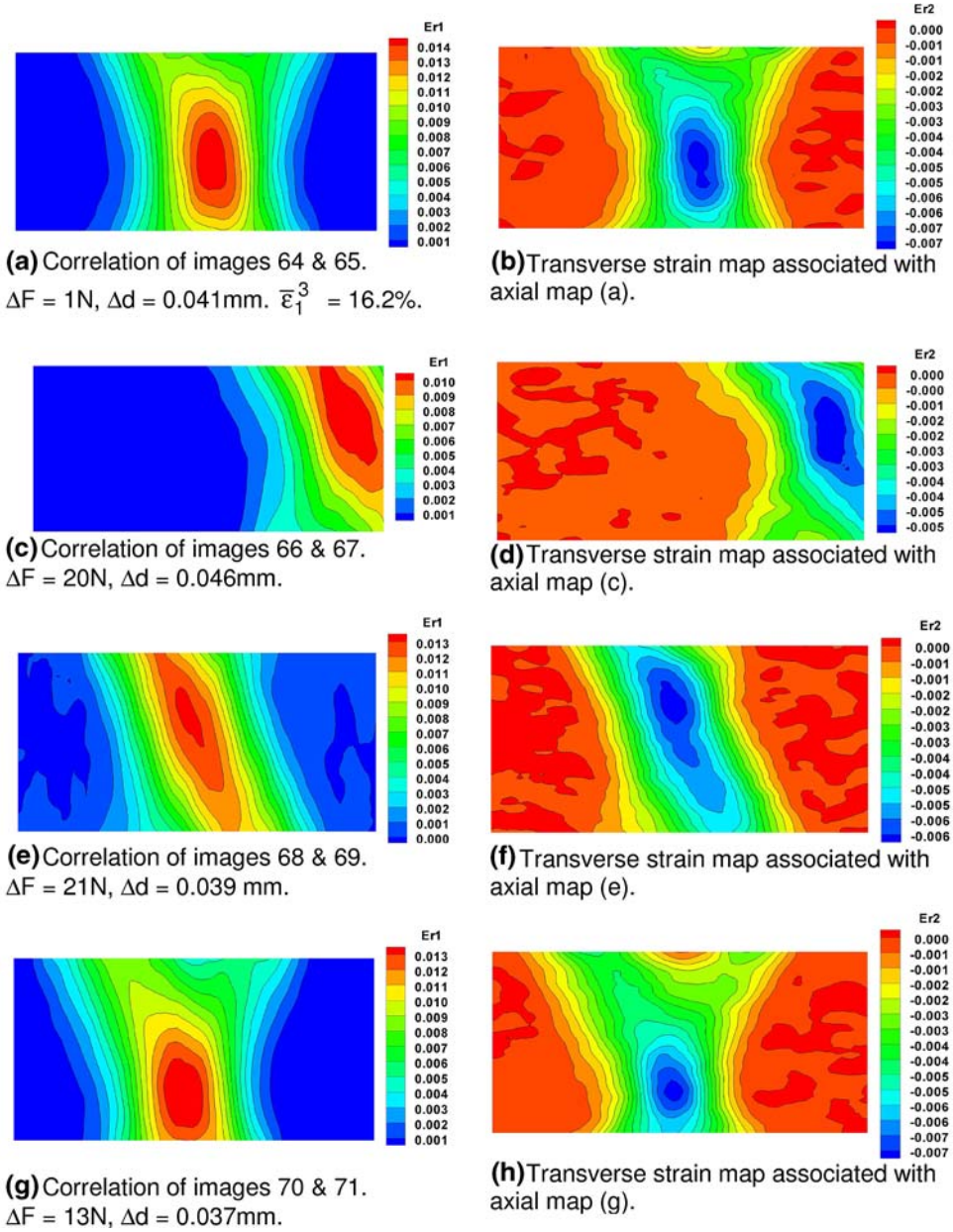

Fig. 5 Selected incremental strain maps from DIC analysis of AA5182-O base material (prior to fracture). Changing positions of peak strain contours from image to image suggest a propagating band of plasticity that is indicative of DSA. Tensile axis is along the horizontal. Er1 = -ΔEr1 and Er2 = ΔEr2 for all incremental maps. (a) Correlation of images 64 and 65. ΔF = 1 N, Δd = 0.041 mm. $\bar{\varepsilon}_1^{(3)}$ = 16.2%; (b) Transverse strain map associated with axial map (a); (c) Correlation of images 66 and 67. ΔF = 20 N, Δd = 0.046 mm; (d) Transverse strain map associated with axial map (c); (e) Correlation of images 68 and 69. ΔF = 21 N, Δd = 0.039 mm; (f) Transverse strain map associated with axial map (e); (g) Correlation of images 70 and 71. ΔF = 13 N, Δd = 0.037 mm; (h) Transverse strain map associated with axial map (g); (i) Correlation of images 74 and 75. ΔF = 2 N, Δd = 0.040 mm; (j) Transverse strain map associated with axial map (i); (k) Correlation of images 78 and 79. ΔF = −7 N, Δd = 0.039 mm; (l) Transverse strain map associated with axial map (k); (m) Correlation of images 80 and 81. ΔF = −11 N, Δd = 0.038 mm. $\bar{\varepsilon}_1^{(3)}$ = 43%; (n) Transverse strain map associated with axial map (m); (o) Correlation of images 86 and 87. ΔF = −37 N, Δd = 0.040 mm; and (p) Transverse strain map associated with axial map (o)

direction of band propagation suggested in Fig. 7(c) to (f) is generally from left to right across each incremental map, this changed with a load increment of 15 N between images 81 and 82 wherein the band moved to the left of center of Fig. 7(g) and (h). The orientation of the band subsequently changed due to a 2 N decrement between images 84 and 85 with corresponding peak axial and transverse strain increments of 1.5% and −0.8%. This is shown in Fig. 7(i) and (j). Although there was some change in the shape of the band with a 6 N decrement between images 87 and 88, as shown in Fig. 7(k) and (l), the band remained positioned at the location it achieved in Fig. 7(i) and (j) with little difference in the associated peak axial and transverse strain increments. Recall that the peak cross-head load was achieved at image 86, and hence the contour patterns in Fig. 7(k) and (l), are associated with a continuous decrease in load. The necking region in the friction stir processed

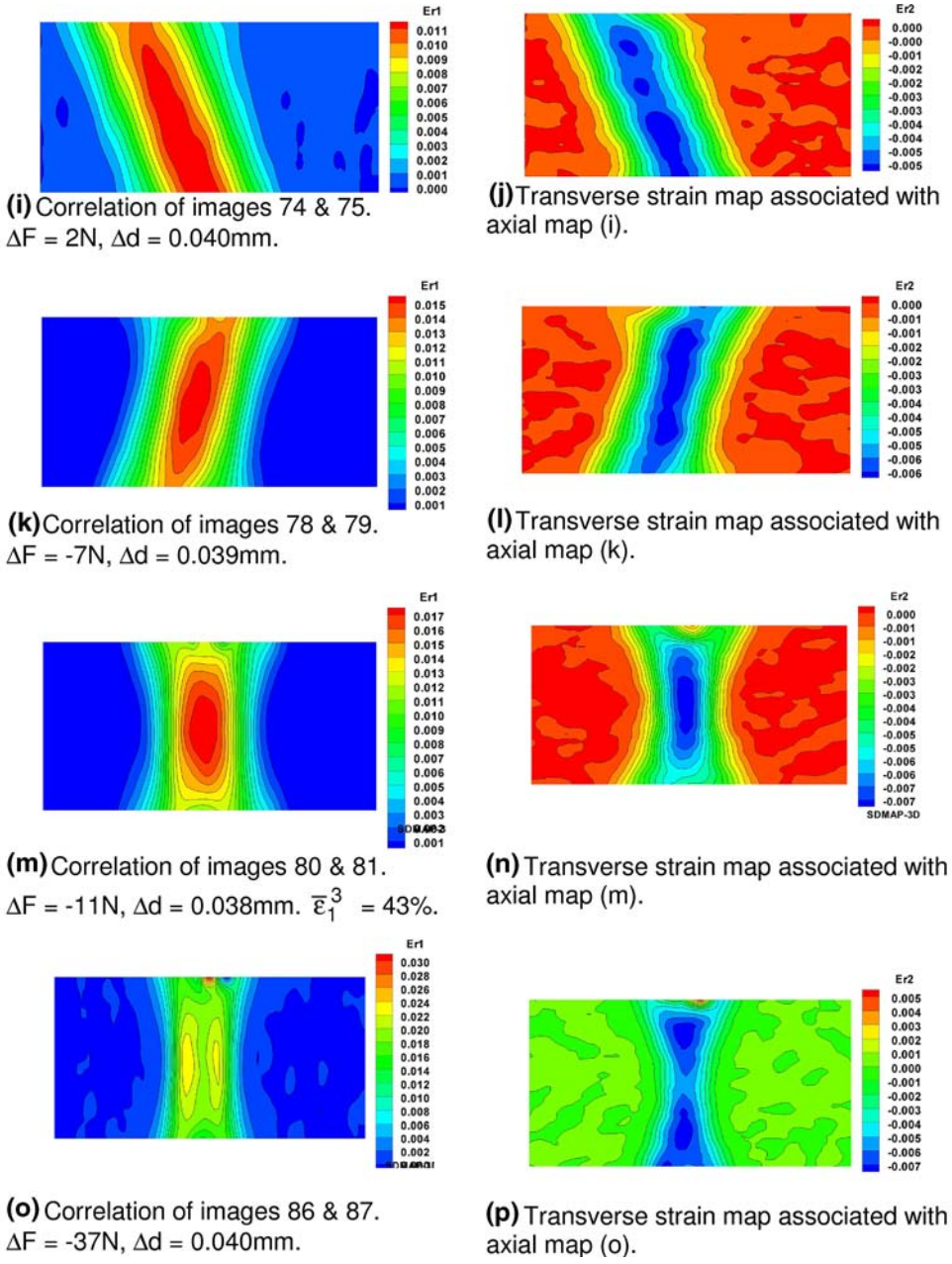

Fig. 5 continued

AA5182-O coupon changed its orientation once again, with a 25 N load decrement between images 92 and 93. The region of axial strain increment thinned down as shown in Fig. 7(m). The region of transverse strain increment tended to be wider, as shown by the blue contour patches in Fig. 7(n). This thinning continued close to the point of fracture, as shown in Fig. 7(o) and (p) (the computed $\bar{\varepsilon}_1^{(3)}$ value of 42% is included in the Fig. 7o caption), for which peak axial and transverse strain increments were 4.0% and −0.8% due to a 58 N load decrement between images 95 and 96. The incremental strain maps in Fig. 7(o) and (p) show significant differences when compared with those of Fig. 5(o) and (p) for the AA5182-O base material. For both materials, however, propagating bands of localized plasticity are observed which we surmise are indicative of dynamic strain aging.

3.2.3 6111-T4: Friction Stir Processed. We noted minimal differences between the cumulative and incremental strain maps computed for the base and friction stir processed AA6111-T4 materials. We therefore focus only on results from the friction stir processed material. For the test of interest here, 100 bitmap images were recorded and the peak cross-head load of 3799 N occurred at image 77. No oscillation in the cross-head load was noted prior to the time when the peak load was reached.

Figure 8(a) to (h) shows selected cumulative strain maps resulting from DIC analysis of images recorded later in the test with the second image recorded after the start of the test. Figure 8(a) to (d) shows the development of a narrow diffuse neck near the coupon center that appears stationary when the load increases from 3806 N to 3784 N between the images

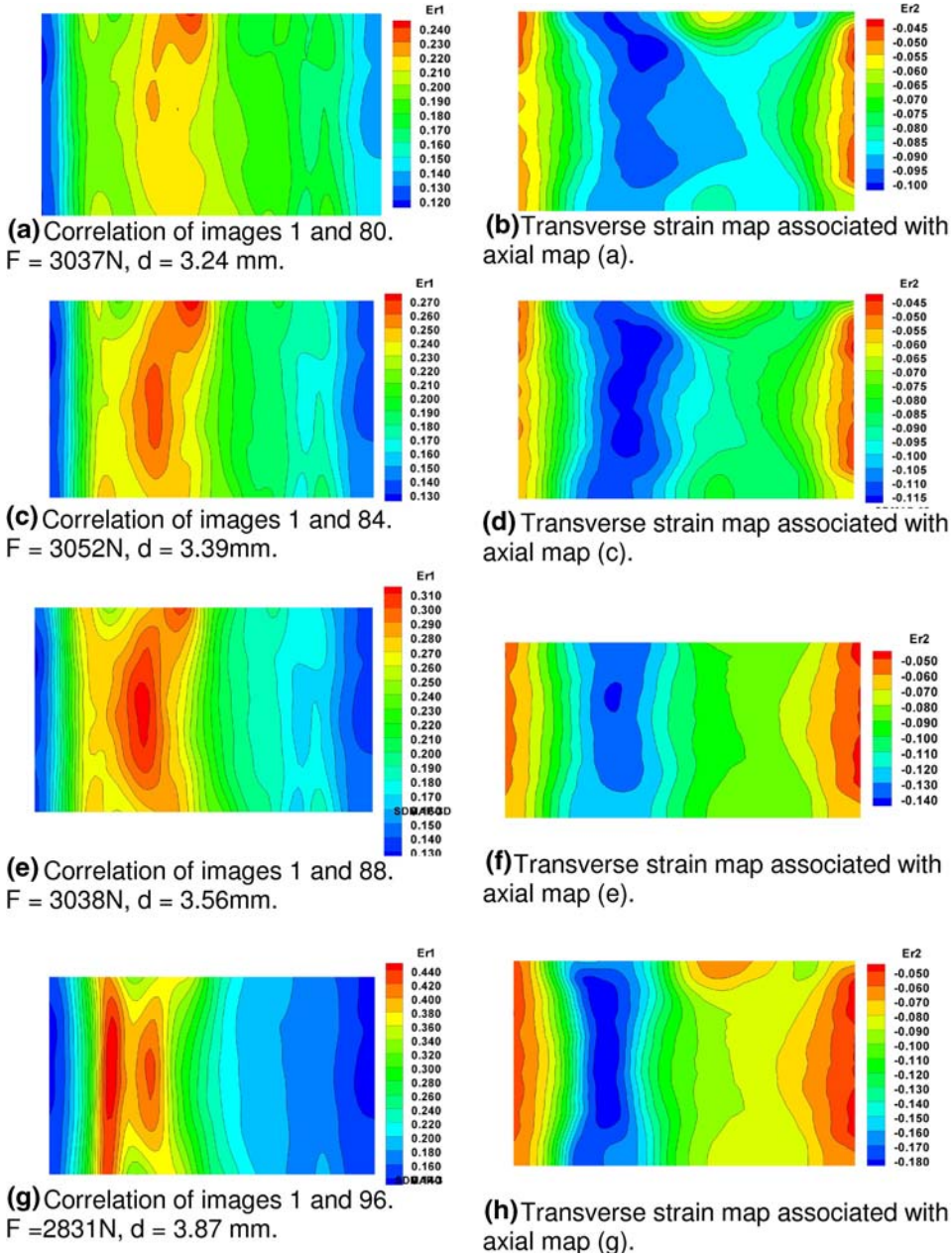

Fig. 6 Selected cumulative strain maps from DIC analysis of AA5182-O friction stir processed material (prior to fracture). Tensile axis is along the horizontal. Corresponding load and cross-head displacement are denoted by F and d, respectively. (a) Correlation of images 1 and 80. F = 3037 N, d = 3.24 mm; (b) Transverse strain map associated with axial map (a); (c) Correlation of images 1 and 84. F = 3052 N, d = 3.39 mm; (d) Transverse strain map associated with axial map (c). (e) Correlation of images 1 and 88. F = 3038 N, d = 3.56 mm; (f) Transverse strain map associated with axial map (e); (g) Correlation of images 1 and 96. F = 2831 N, d = 3.87 mm; and (h) Transverse strain map associated with axial map (g)

associated with Fig. 8(a, b) and Fig. 8(c, d). Figure 8(a) and (b) corresponds to the 3806 N load and show peak axial and transverse strain levels of 23% and −10.5% respectively. The peak axial strain in Fig. 8(c) increased to 28% (red contours), while the peak transverse strain dropped to −13%. Beyond the peak load, a minimal change to the necking region occurred, although the peak axial strain jumped to 38%, as shown in Fig. 8(e), and the peak transverse strain falls to −18%, as shown in Fig. 8(f). The accumulated axial strain reached 50% just prior to fracture, as shown in the red contour patches of Fig. 8(g). The contour shapes in Fig. 8(g) are dramatically different those of Fig. 6(g) for the friction stir processed AA5182-O material, a difference that is likely due to dynamic strain aging in the latter material. Accumulated transverse strains fall to −24%, as shown in the blue contour strip in Fig. 8(h).

In stark contrast to the incremental strain maps examined for the AA5182-O materials, those displayed in Fig. 9 do not suggest a propagating band of localized plasticity. There are two possible reasons for this. One is that the dynamic strain aging effect may not occur in the AA6111-T4 alloy (although there is indication from the literature that it occurs in some Al-Si alloys (Ref 17)). The other reason may be that the bands may in fact propagate, but perhaps at a rate that could not be adequately

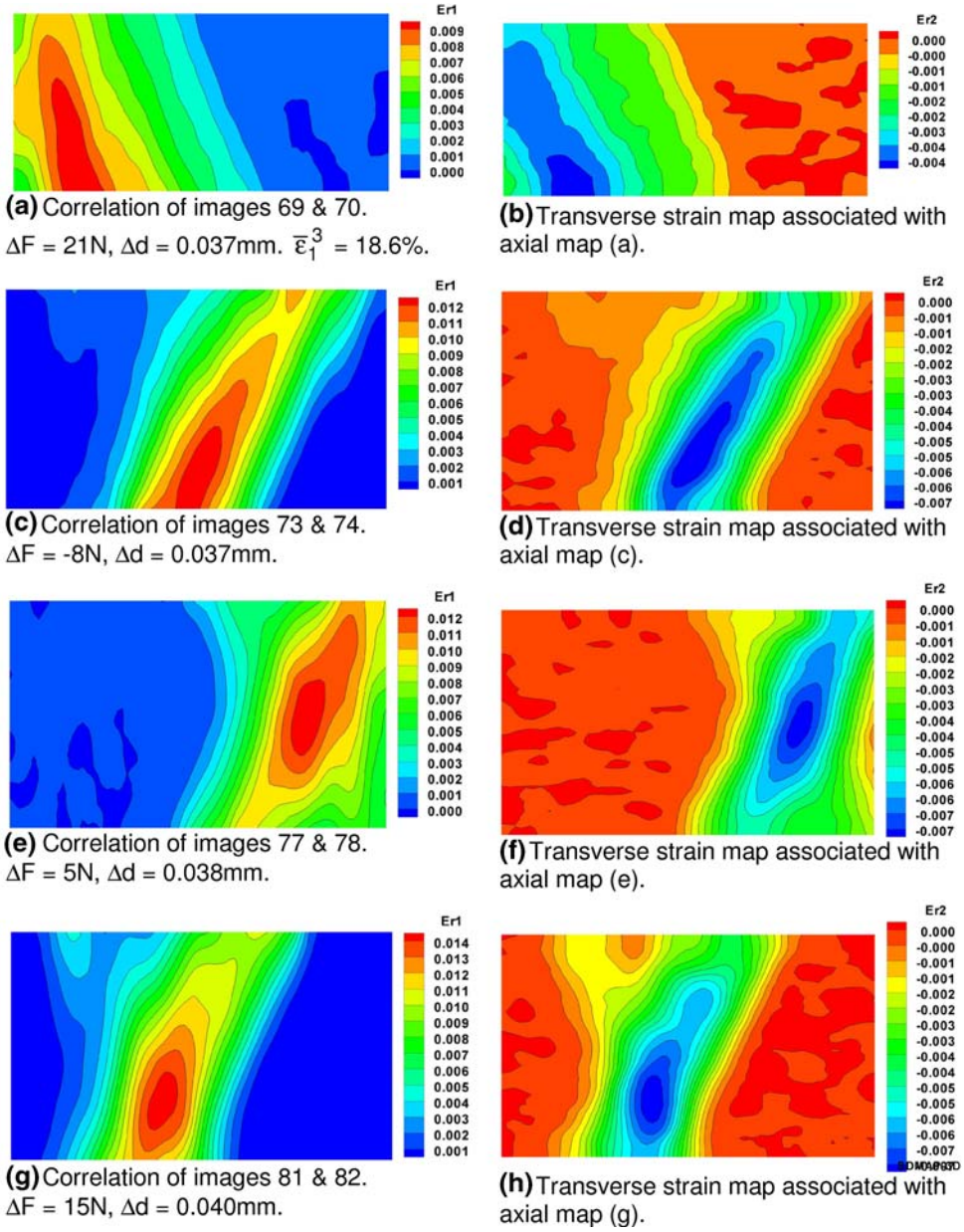

Fig. 7 Selected incremental strain maps from DIC analysis of AA5182-O friction stir processed material (prior to fracture). Varying positions of peak strain contours from image to image suggest a propagating band of plasticity. Tensile axis is along the horizontal. Er1 = ΔEr1 and Er2 = ΔEr2 for all incremental maps. (a) Correlation of images 69 and 70. ΔF = 21 N; Δd = 0.037 mm. $\bar{\varepsilon}_1^{(3)}$ = 18.6%; (b) Transverse strain map associated with axial map (a); (c) Correlation of images 73 and 74. $\Delta F = -8$ N, Δd = 0.037 mm; (d) Transverse strain map associated with axial map (c); (e) Correlation of images 77 and 78. ΔF = 5 N, Δd = 0.038 mm; (f) Transverse strain map associated with axial map (e); (g) Correlation of images 81 and 82. ΔF = 15 N, Δd = 0.040 mm; (h) Transverse strain map associated with axial map (g); (i) Correlation of images 84 and 85. $\Delta F = -2$ N, Δd = 0.039 mm; (j) Transverse strain map associated with axial map (i); (k) Correlation of images 87 and 88. $\Delta F = -6$ N, Δd = 0.039 mm; (l) Transverse strain map associated with axial map (k); (m) Correlation of images 92 and 93. $\Delta F = -25$ N, Δd = 0.040 mm; (n) Transverse strain map associated with axial map (m); (o) Correlation of images 95 and 96. $\Delta F = -58$ N, Δd = 0.040 mm. $\bar{\varepsilon}_1^{(3)}$= 42%; and (p) Transverse strain map associated with axial map (o)

captured with the imaging and data acquisition systems used in this investigation. A narrow, diffuse neck is shown in the incremental axial contour map in Fig. 9(a) due to a load increase of 1 N between images 71 and 72. Contours of the transverse strain increment are somewhat broader in Fig. 9(b), as suggested by the blue-green regions. A 4 N load decrement from the peak load results in minimal change to the peak axial strain increment contours as shown in Fig. 9(c) which resulted from correlation of images 77 and 78. A similar observation applies for the contours of transverse strain increment in Fig. 9(d). A 19 N load decrement between images 87 and 88 led to an increase in the size of the peak axial strain increment, as suggested by the large red contour patch in Fig. 9(e). Alternatively, contours of peak transverse strain increment narrowed somewhat as suggested by the blue patches in Fig. 9(f). Finally, a 51 N load decrement between images 97 and 98, which occurs

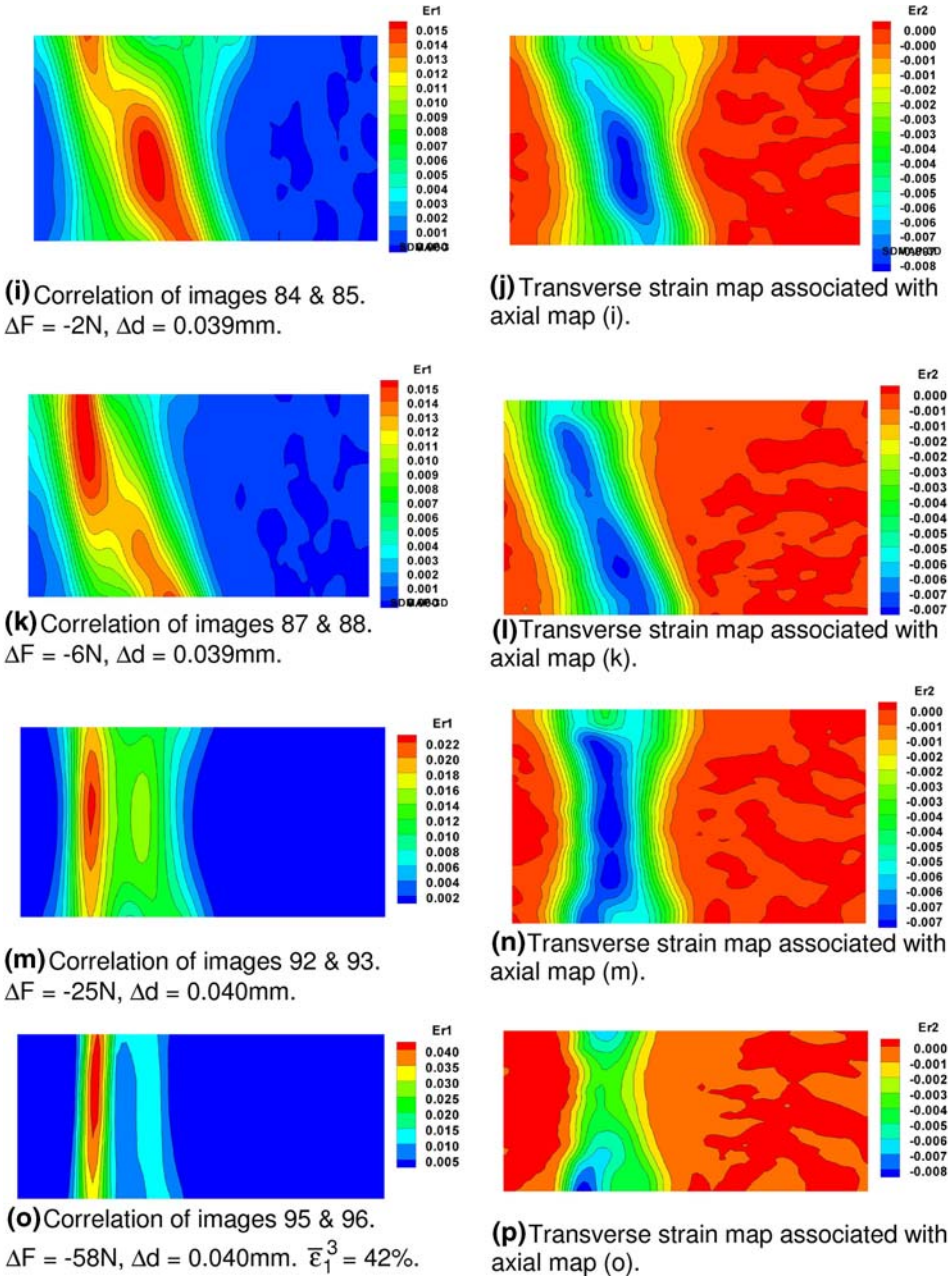

Fig. 7 continued

right before fracture, represents a 1.8% increment in the axial strain as shown in the contour map of Fig. 9(g). Incremental values associated with the blue contours in Fig. 9(g) remain close to what they were in Fig. 9(a). Interestingly, transverse strain increment contours suggest a local increase in Fig. 9(f) to −0.6% (cf. the blue contour patch in Fig. 9(b)). Regions of peak transverse strain increment become localized to the edges of the gage section as denoted by the blue contour patches above and below the green contour patch in Fig. 9(h).

4. Grain Size, Texture and Precipitation Effects on Strength

As shown in Fig. 20 of Part 1, nominal grain size variation in the AA5182-O friction stir processed zone is very minimal from the top of the zone (i.e., that came into contact with the tool) to the bottom. The average grain size is close to 4 μm. Alternatively, there is generally a much a larger grain size variation in the AA6111-T4 material: this develops a larger grain size than the AA5182-O alloy and a stronger texture during friction stir processing. The largest grain size (around 10 μm) occurs between 1.0 and 1.5 mm from the top surface of the material.

Both friction stir processed materials exhibit a strength increase compared to the unprocessed materials. This can be attributed to three factors: (a) grain refinement, (b) texture modification, and (c) precipitation/aging. The dominant effect on strength in both friction stir processed alloys is likely the refinement of grain size, with (b) and (c) playing secondary roles. Measured yield strengths vs. grain sizes for standard AA5182-O and AA5754-O confirm this (Ref 18). Friction stir

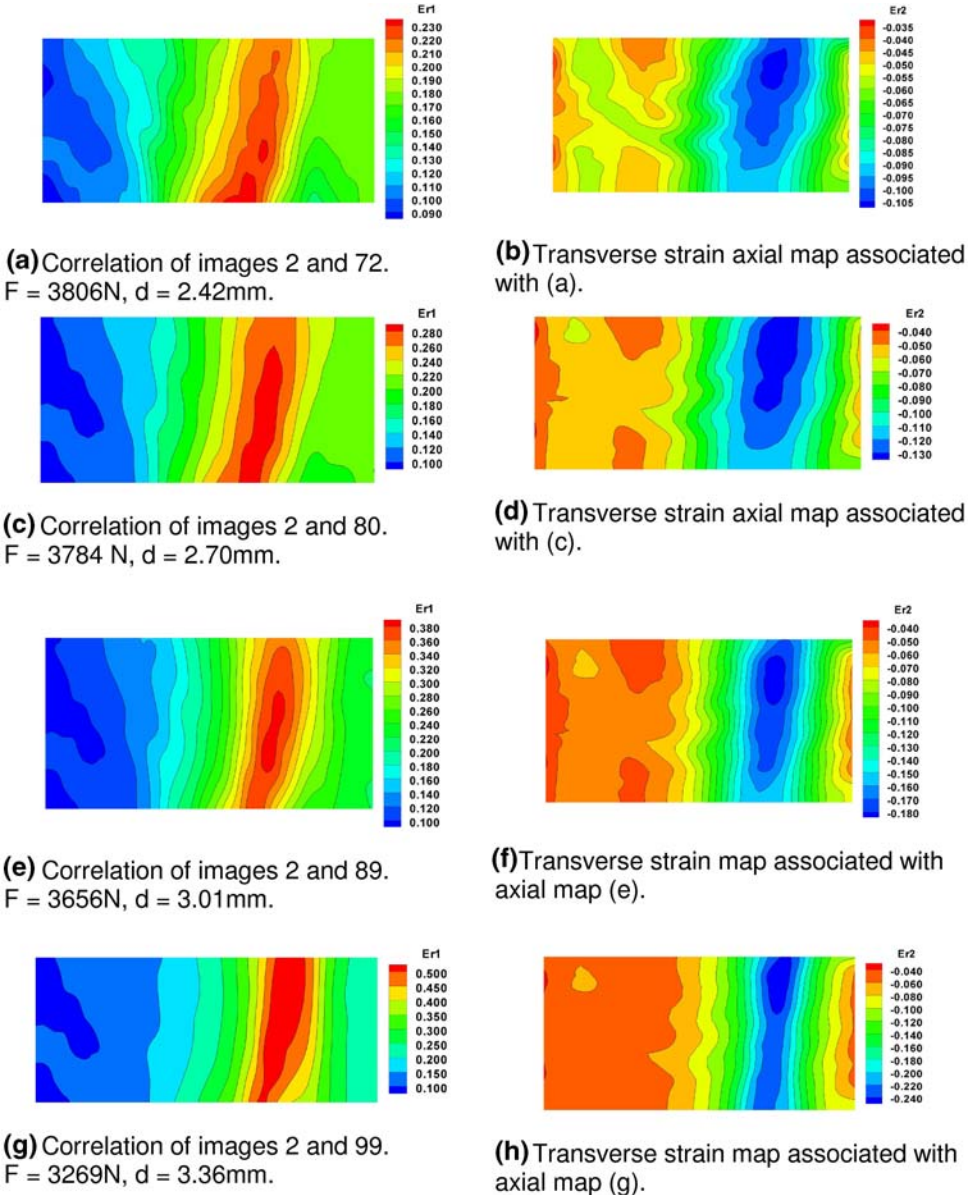

Fig. 8 Selected cumulative strain maps from DIC analysis of AA6111-T4 friction stir processed material (prior to fracture). Tensile axis is along the horizontal. Corresponding load and cross-head displacement are denoted by F and d, respectively. (a) Correlation of images 2 and 72. F = 3806 N, d = 2.42 mm; (b) Transverse strain axial map associated with (a); (c) Correlation of images 2 and 80. F = 3784 N, d = 2.70 mm; (d) Transverse strain axial map associated with (c); (e) Correlation of images 2 and 89. F = 3656 N, d = 3.01 mm; (f) Transverse strain map associated with axial map (e); (g) Correlation of images 2 and 99. F = 3269 N, d = 3.36 mm; and (h) Transverse strain map associated with axial map (g)

processing generates a thermal field that can lead either to dissolution or coarsening of local precipitate microstructure followed by natural aging. These factors can have a complex effect on strength. Clearly, a direct quantitative linkage between the texture measurements in Part 1 and the tensile properties measured on the entire friction stir processed zones of both alloys is problematic due to the local texture variations noted therein.

In order to elucidate the effect of friction stir processing on aging/precipitation, further experiments in which AA5182-O and AA6111-T4 coupons are heat treated to an overaged condition, or to a W or solution treated condition are required and re-examine mechanical behavior. This would eliminate any microstructural inhomogeneity caused by the heat from the friction stir processing. Following texture characterization with EBSD, miniature tensile coupons could then be prepared from regions of differing texture and the mechanical properties once again measured with digital image correlation.

5. Conclusions

The evolution of two-dimensional strain fields during tensile tests of base and friction stir processed AA5182-O and AA6111-T4 materials was investigated with a state-of-the-art digital image correlation method with custom image and data acquisition systems. Specially fabricated coupons were strained

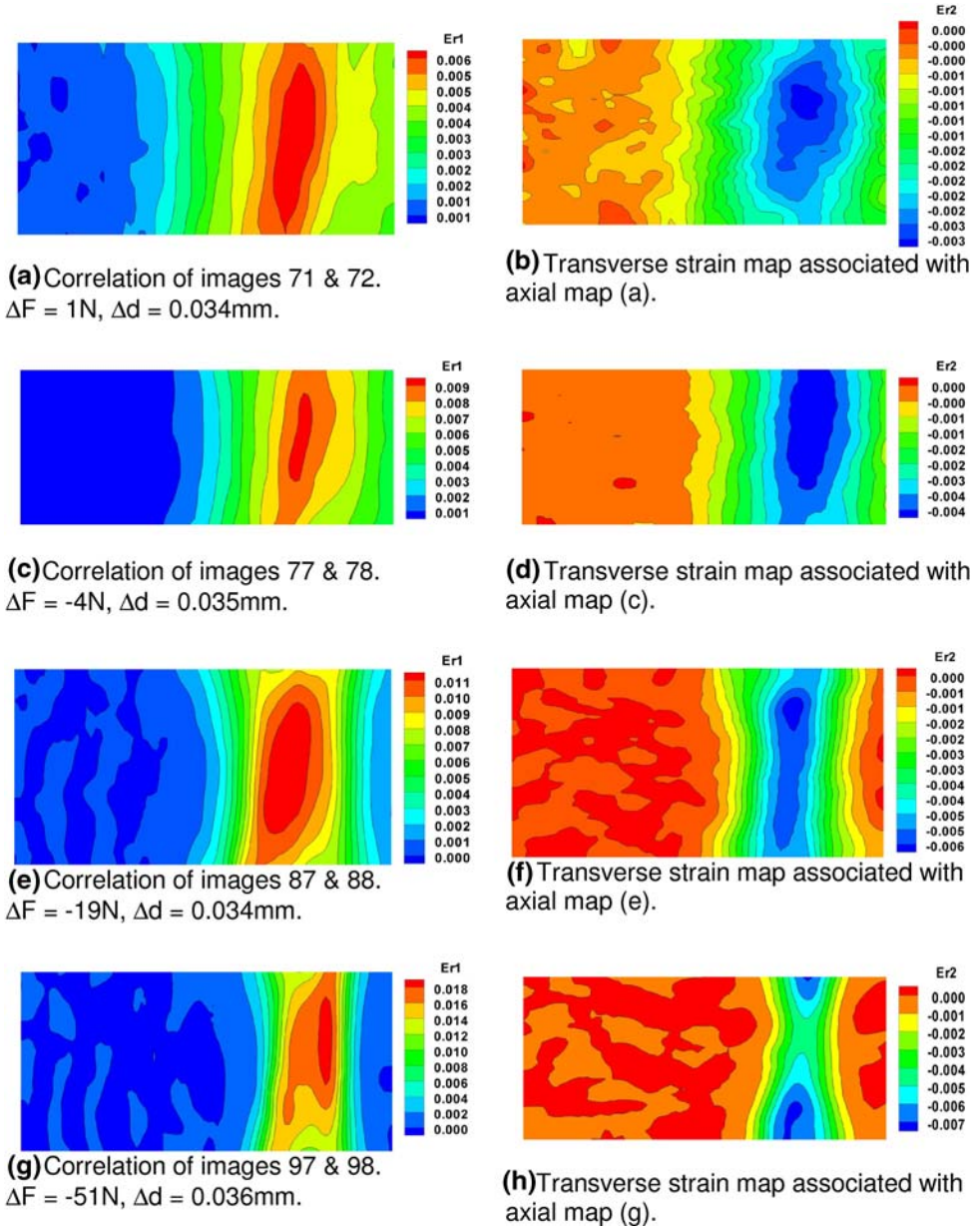

Fig. 9 Selected incremental strain maps from DIC analysis of AA6111-T4 friction stir processed material (prior to fracture). Tensile axis is along the horizontal. Er1 = ΔEr1 and Er2 = ΔEr2 for all incremental maps. (a) Correlation of images 71 and 72. $\Delta F = 1$ N, $\Delta d = 0.034$ mm; (b) Transverse strain map associated with axial map (a); (c) Correlation of images 77 and 78. $\Delta F = -4$ N, $\Delta d = 0.035$ mm; (d) Transverse strain map associated with axial map (c); (e) Correlation of images 87 and 88. $\Delta F = -19$ N, $\Delta d = 0.034$ mm; (f) Transverse strain map associated with axial map (e); (g) Correlation of images 97 and 98. $\Delta F = -51$ N, $\Delta d = 0.036$ mm; and (h) Transverse strain map associated with axial map (g)

to fracture in a miniature tensile stage. True stress-true strain curves were computed for all four material types using strain measures that are suitable uniaxial representations of two-dimensional strain fields. The strain fields are computed from digital grids superimposed onto each image recorded from one surface of the coupon during tensile testing. We note that the friction stir processed AA5182-O material has a 0.2% yield stress that only slightly exceeds that of the base material. The difference in yield strengths for the AA6111-T4 base and friction stir processed materials was found to be in excess of 10 MPa with the latter material having the higher yield stress. Larger differences in the ultimate tensile strengths between the two material types were noted. Again, the friction stir processed material exhibited ultimate tensile strength values in excess of the corresponding base material. This was reflected in the computed true stress-true strain curves plotted for each material. The friction stir processed AA6111-T4 accumulated the largest tensile strains prior to fracture. To investigate possible differences in the strain evolution during tensile deformation between the different materials, we computed a series of strain maps which are contours of constant strain derived from surface displacements computed directly from the digital grids. Both incremental and cumulative strain maps were examined, with the former showing a propagating band of

localized plasticity in both the AA5182-O base and friction stir processed materials. Perhaps the most significant difference between these materials as revealed by the incremental strain maps is that just prior to fracture. The friction stir processed material localized strains in a very narrow band along the gage section. No band propagation was noted for either of the AA6111-T4 materials.

Since we have previously explored texture variations in AA5182-O and AA6111-T4 materials, a possible next step along the path to linking texture and mechanical properties would be to extract miniature tensile coupons from regions of each material with significant texture. Key tensile properties of the coupons could then be measured with/computed from the DIC method. This follows the same approach used to investigate tensile properties of different zones in dual-phase steel spot welds (Ref 8).

6. Appendix

Four definitions of the average axial true strain measures were employed in this study. The corresponding mathematical definitions of the average strain measures are as follows:

$$\bar{\varepsilon}_1^{(1)} = \frac{1}{MN}\sum_{j=1}^{N}\sum_{i=1}^{M}\varepsilon_1(i,j), \qquad \text{(Eq A1)}$$

where $\bar{\varepsilon}_1^{(1)}$ is the axial strain averaged over the entire gage section (following the conventional tensile test methodology), M and N are the total numbers of grid points along the gage length and width directions, respectively, and $\varepsilon_1(i,j)$ is the local axial strain at each grid point (i, j) obtained via DIC;

$$\bar{\varepsilon}_1^{(2)} = \frac{1}{M_n N}\sum_{j=1}^{N}\sum_{i=M_1}^{M_1+M_n}\varepsilon_1(i,j), \qquad \text{(Eq A2)}$$

where $\bar{\varepsilon}_1^{(2)}$ is the axial strain averaged over the entire neck region (this is the lower bound estimate of average strain in the diffuse neck), M_1 and M_n are the starting and total number of grid points along the gage length direction of the neck region, respectively;

$$\bar{\varepsilon}_1^{(3)} = \frac{1}{N}\sum_{j=1}^{N}\varepsilon_1(M_0,j), \qquad \text{(Eq A3)}$$

where $\bar{\varepsilon}_1^{(3)}$ is the axial strain averaged along the bar cross-section with the smallest width (i.e., the neck center line at $i = M_0$);

$$\bar{\varepsilon}_1^{(5)} = \varepsilon_1(M_0,N_0) = \max_{j=1,N}[\varepsilon_1(M_0,j)], \qquad \text{(Eq A4)}$$

where $\bar{\varepsilon}_1^{(5)}$ is the maximum axial strain at the center of a diffuse neck corresponding to the grid point (M_0, N_0). This definition of axial strain provides the upper bound estimate of measurable average strain in the diffuse neck. Since the entire gage section was used to compute $\bar{\varepsilon}_1^{(1)}$, local strain heterogeneities were averaged-out over the gage section. Alternatively, the strain fields selected for computing $\bar{\varepsilon}_1^{(2)}$, $\bar{\varepsilon}_1^{(3)}$, and $\bar{\varepsilon}_1^{(5)}$, were measured over the entire neck region, or a selected part of the neck region, and hence local strain heterogeneities were more accurately quantified. Both analytical and numerical analyses have shown that the average axial true strains $\bar{\varepsilon}_1^{(2)}$ and $\bar{\varepsilon}_1^{(3)}$ as defined, respectively, by Eq (A3) and (A4) are the most accurate estimates (Ref 11) of *uniaxial* true strain and true stress (via Eq 1) beyond diffuse necking in various tensile bar geometries. The definitions $\bar{\varepsilon}_1^{(1)}$ and $\bar{\varepsilon}_1^{(5)}$ provide uniaxial true stress-strain curves that bound the actual uniaxial true stress-strain curve irrespective of tensile bar geometry.

References

1. S. Agarwal, C.L. Briant, L.G. Hector, Jr., and Y.-L. Chen, Friction Stir Processed AA5182-O and AA6111-T4 Aluminum Alloys. Part 1: Electron Backscattered Diffraction Analysis. *J. Mater. Eng. Perform.*, 2007, in press
2. A.J. Schwartz, M. Kumar, and B.L. Adams, *Electron Backscatter Diffraction in Materials Science*. Kluwer Academic/Plenum Publishers, New York (NY), 2000
3. L.G. Hector Jr., Y.-L. Chen, S. Agarwal, and C.L. Briant, Texture Characterization of Autogenous Nd: YAG Laser Welds in AA5182-O and AA6111-T4 Aluminum Alloys, *Metall. Mater. Trans. A*, 2004, **35**, p 3032–3037
4. W.D. Lockwood and A.P. Reynolds, Simulation of the Global Response of a Friction Stir Weld using Local Constitutive Behavior, *Mater. Sci. Eng. A*, 2003, **339**, p 35–42
5. M.A. Sutton, B. Yang, A.P. Reynolds, and J. Yan, Banded Microstructure in 2024-T351 and 2524-T351 Aluminum Friction Stir Welds Part II. Mechanical Characterization, *Maters. Sci. Eng. A*, 2004, **364**, p 66–74
6. http://www.kammrath-weiss.com/english/about_us/unshome.htm
7. http://www.dasylab.net/dasylab_english/
8. W. Tong, H. Tao, X. Jiang, N. Zhang, M. Marya, L.G. Hector Jr., and X.Q. Gayden, Deformation and Fracture of Miniature Tensile Bars with Resistance Spot-Weld Microstructures, *Metall. Mater. Trans.*, 2005, **36**, p 2651–2669
9. W. Tong, H. Tao, N. Zhang, and L.G. Hector Jr., Time-Resolved Strain Mapping Measurements of Individual Portevin-Le Châtelier Deformation Bands, *Scripta Mater.*, 2005, **53**, p 87–92
10. W. Tong, "A User's Guide to the Yale Surface Deformation Mapping Program (SDMAP)," Technical Report, Yale University, New Haven, CT, 1996–2004
11. B.W. Smith, X. Li, and W. Tong, Error Assessment for Strain Mapping by Digital Image Correlation, *Exp. Tech.*, 1999, **22**, p 19–21
12. M.P. Miles, B.J. Decker, and T.W. Nelson, Formability and Strength of Friction-Stir-Welded Aluminum Sheets, *Metall. Mater. Trans. A*, 2004, **35**, p 3461–3468
13. X. Long, "Finite Element Analysis of Residual Stress Generation During Spot Welding and Its Effect on Fatigue Behavior of Spot Welded Joints," Ph.D. Dissertation, Mechanical Eng. Dept., University of Missouri-Columbia, 2005. Available on-line at: http://edt.missouri.edu/Fall2005/Dissertation/LongX-120605 D3393/research.pdf#search = %22yield%20strength%206111-T4%22]
14. J.F. Bell, The Experimental Foundations of Solid Mechanics, *Mechanics of Solids I. Encyclopedia of Physics*, vol. 1, S. Flügge and C. Truesdell, Eds., Springer-Verlag, New York, 1973
15. Y. Estrin and L.P. Kubin, Spatial Coupling and Propagative Plastic Instabilities, *Continuum Models for Materials with Microstructures*, H.B. Mühlhaus, Ed., Wiley, New York, 1995, p 395–450
16. P. Hähner, On the Physics of the Portevin-Le Châtelier Effect Part 1: The Statistics of Dynamic Strain Ageing, *Mater. Sci. Eng. A*, 1996, **207**, p 208–215
17. J.M. Robinson, Serrated Flow in Aluminum Alloys, *Int. Mater. Rev.*, 1994, **39**, p 217–227
18. P.N. Anyalebechi, "Materials Science and Engineering Laboratory Manual," School of Engineering, Padnos College of Engineering and Computing, Grand Valley State University, Jan. 2005, p 98–101